PAPER • OPEN ACCESS

Investigating the role of edge neutrals in exciting tearing mode activity and achieving flat temperature profiles in LTX-β

To cite this article: Santanu Banerjee *et al* 2024 *Nucl. Fusion* **64** 046026

View the article online for updates and enhancements.

Investigating the role of edge neutrals in exciting tearing mode activity and achieving flat temperature profiles in LTX-β

Santanu Banerjee[1,*] ⓘ, D.P. Boyle[1] ⓘ, A. Maan[1] ⓘ, N. Ferraro[1] ⓘ, G. Wilkie[1], R. Majeski[1] ⓘ, M. Podesta[1] ⓘ, R. Bell[1] ⓘ, C. Hansen[2] ⓘ, W. Capecchi[3] ⓘ and D. Elliott[4] ⓘ

[1] Princeton Plasma Physics Laboratory, PO Box 451, Princeton, NJ 08542-0451, United States of America
[2] Department of Aeronautics and Astronautics, University of Washington, Seattle, WA 98195, United States of America
[3] University of Wisconsin-Madison, Madison, WI 53706-1687, United States of America
[4] Oak Ridge National Laboratory, Oak Ridge, TN 37830, United States of America

E-mail: sbanerje@pppl.gov

CrossMark

Abstract

We present observations, numerical simulations, and analysis from experiments in the Lithium Tokamak Experiment-Beta (LTX-β) in which the electron temperature profile ($T_e(r)$) shifts from flat to peaked and a tearing mode is also destabilized when the average density (n_e^{ave}) exceeds $\sim 10^{19}$ m^{-3}. Flat $T_e(r)$ is obtained routinely in LTX-β, with a lithium coated, low-recycling first wall, once the external fueling is stopped and density decays [Boyle *et al* 2023 *Nucl. Fusion* **63** 056020]. In the present experiment, flat T_e profiles can be sustained while maintaining constant n_e^{ave} below a line averaged density threshold ($n_e^{ave}_{th}$) of $\sim 10^{19}$ m^{-3}. Above $n_e^{ave}_{th}$, $T_e(r)$ shifts from flat to peaked and a tearing mode is destabilized. Due to low recycling, the achieved n_e^{ave} can be controlled precisely by external fueling and hence, a certain threshold of the edge neutral inventory from the external fueling is experimentally manifested through $n_e^{ave}_{th}$. The goal of the present work is to investigate the role of edge neutrals in determining $T_e(r)$ and MHD stability in the unique low-recycling regime of LTX-β. Our hypothesis is that the peaking of $T_e(r)$ beyond $n_e^{ave}_{th}$ is due ultimately to the edge cooling by the cold neutrals beyond a critical fueling flux. At lower fueling flux, flat $T_e(r)$ results in broader pressure profile and lower resistivity, which in turn stabilizes the tearing mode. This hypothesis is supported by edge neutral density estimation by DEGAS 2 code. Mode analysis by singular value decomposition confirms the tearing mode structure to be $m/n = 2/1$ (m and n being the poloidal and toroidal mode numbers). Linear tearing stability analysis with M3D-C1 predicts that plasmas with $n_e^{ave} > 10^{19}$ are highly susceptible to a $n = 1$ tearing mode. ORBIT simulations, however, confirmed that the tearing modes do not contribute to the loss of fast ions

---

* Author to whom any correspondence should be addressed.

from neutral beam injection. This study shows for the first time that the neutral inventory at the edge could be one of the deciding factors for the achievability of the unique operation regime of flat $T_e(r)$ and the excitation of tearing activity that could be disruptive for the plasmas.

Keywords: edge cooling, density control, tokamak, low recycling, MHD stability

(Some figures may appear in colour only in the online journal)

1. Introduction

It has been reported that flat electron temperature ($T_e(r)$) profiles were obtained in Lithium Tokamak Experiment (LTX) [1] and later in the upgraded Lithium Tokamak Experiment-Beta (LTX-β) tokamak [2, 3], with a lithium coated first wall. Due to strong hydrogen retention and lower recycling of lithium, edge cooling can be minimized, and the plasma is thermally decoupled from the wall, permitting the edge temperature to approach the core temperature [4]. The resulting low or zero temperature gradients eliminate thermal conduction, and energy losses become limited by particle diffusion [5, 6]. Reduction or elimination of the core temperature gradient removes the temperature gradient driven instabilities like micro-tearing mode [7–9], electron and ion temperature gradient modes [10–14]. Remaining sources of instability drive include the density gradient [15, 16], and velocity space anisotropies due to trapped particles [17–19]. With temperature gradient driven instabilities being minimized and a bigger and hotter temperature core, one can expect better confinement and larger fusion volume, which can aid the viability of the commercialization of fusion power.

In order to avoid the edge cooling effect by the cold edge neutrals from wall recycling (which is suppressed in LTX-β) and/or from the external fueling, flat T_e profiles were obtained earlier with very low density once the external fueling is stopped [1]. However, for better plasma performance and for any attempt of coupling neutral beam power to the plasma, higher density operation is desirable. But, with increased fueling for increasing the plasma density, one can expect a reduction in the edge temperature due to edge cooling by the cold neutrals puffed at the edge.

Edge cooling can pose another challenge for achieving better performing plasmas. In the scenario of edge cooling and associated current profile contraction, excitation of $m/n = 2/1$ tearing modes, where m and n are poloidal and toroidal mode numbers respectively, has been reported in several tokamaks worldwide [20–30]. Often the 2/1 mode is coupled with 3/1 or 3/2 modes. If these modes are allowed to grow and lock, that can cause sudden loss of confinement and eventually plasma disruption [20, 21, 28]. Rebut and Hugon [31] proposed a plausible explanation of this phenomenon of tearing mode excitation by edge cooling by invoking an extension to the classical model of tearing modes where the modes are being solely driven by current gradients. This extension considers a thermal instability that can cause island cooling by radiation and that in turn increased resistivity inside the island. As a result, the island grows due to an enhancement in the helical perturbation current. Later the Rutherford equation is extended [32] with a radiation term and exponential growth of the island is predicted. This phenomenology was confirmed by the experiments on Rijnhuizen Tokamak Project [33].

The goal of the present work is to investigate the role of edge neutrals in exciting the tearing activity and achieving flat T_e profiles in LTX-β. It is observed in LTX-β that beyond a line averaged density threshold ($n_e{}^{ave}{}_{th}$) of $\sim 10^{19}$ m^{-3}, the T_e profile shifts from flat to peaked and a tearing mode is also destabilized. Due to low recycling, the achieved $n_e{}^{ave}$ can be controlled precisely by external fueling by either high field side gas puffing (HFS-GP) and/or supersonic gas injection (SGI) and hence, essentially a certain threshold of the edge neutral inventory from the external fueling is experimentally manifested through $n_e{}^{ave}{}_{th}$ for tearing mode destabilization. Understanding the criteria for the excitation of the tearing modes is important as there are ongoing efforts in LTX-β to optimize the achievability of the novel operation regime of flatter T_e profile, at higher and sustained densities with suitably tailored fueling. As one of the objectives of operating at higher density is to ensure better coupling and efficient heating by neutral beam injection (NBI), loss of the fast ions from the neutral beam, due to the tearing activity, is also evaluated. Once it is established that indeed the edge cooling through cold neutrals at the edge, provided via edge fueling, is responsible for the destabilization of the tearing mode as well as shift of the T_e profile from flat to peaked, scenarios where core fueling is achieved by either NBI or pellet injection may suggest achievability of flat T_e profile at reactor relevant densities.

It is worthwhile to note here that lithium as a first wall will be liquid in a reactor. Hence, extremely high edge temperatures would indeed be part of the proposed low-recycling reactor approach, while the unique properties of liquid lithium would make it feasible, as discussed in previous works [5, 6, 34].

The paper is organized as follows. The experimental setup is detailed in section 2 with emphasis on the LTX-β tokamak machine components, diagnostic suite available for the study, fueling options and the plasma parameters of the representative shots. In section 3, observation of the tearing mode excitation and the mode characteristics are described. Neutral inventory at the edge is evaluated with the DEGAS 2 code in section 4. MHD stability analysis in different operation scenarios of the experiment is performed using the M3D-C1 code in section 5. The effect of the tearing activity on the fast ions is investigated with the ORBIT-Kick code in section 6 and finally the results are summarized and discussed in section 7.
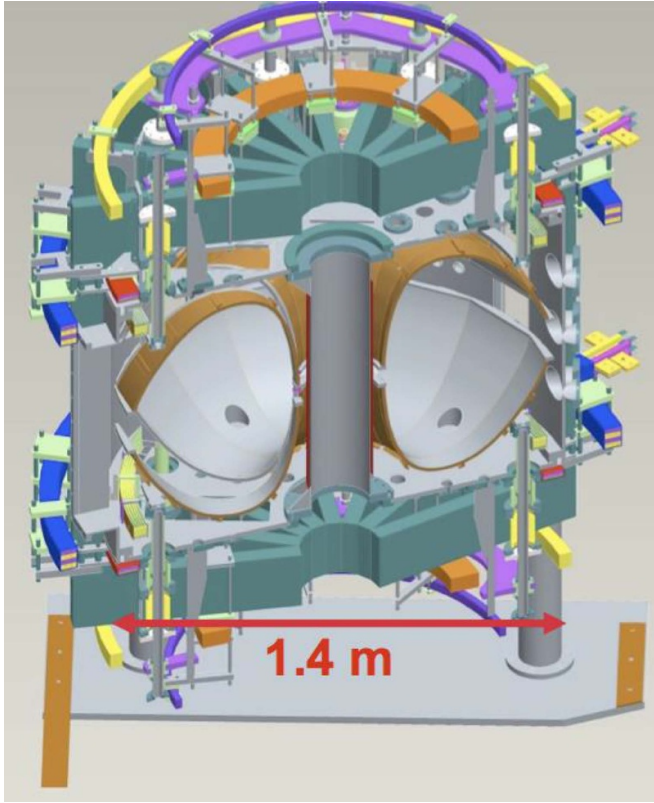
Figure 1. Elevation of LTX-β. The shell is visible, with the inner and outer toroidal gaps indicated, as well as one of the two poloidal cuts (the two poloidal cuts are 180° apart). The poloidal field coils, other than the Ohmic coil system, are color coded as blue, yellow, red, green etc.

2. Experimental setup

2.1. The LTX-β tokamak

The LTX-β spherical tokamak, upgraded from its predecessor LTX, has major radius $R_0 = 40$ cm, minor radius $a = 26$ cm (for an aspect ratio $A = 1.6$), elongation $\kappa = 1.6$, and modest triangularity $\delta = 0.2$–0.4. It has a toroidal field of 3 kG on the axis. The maximum plasma current achieved so far is 135 kA with the help of an expanded Ohmic power supply [3]. A shell, constructed in four segments of a 1.5 mm stainless steel liner explosively bonded to 1 cm thick copper, serves as the first wall to the plasma. The shell is designed to accept interior, plasma-facing coatings of lithium over the high-Z stainless steel substrate. No low-Z materials (e.g. carbon) are employed in the construction. The LTX-β plasma is not magnetically diverted, but limited on the high-field side, lithium-coated surface, of the shell. Primary access for diagnostics is through the outer toroidal gap between shells. Full poloidal access is provided at the two poloidal gaps in the shell structure. An engineering view of LTX-β is shown in figure 1.

2.2. The relevant diagnostic suite for this experiment

There are 10 Mirnov probes in the toroidal array to measure the poloidal magnetic fluctuations [35]. Further, there are 20 three-axes probes in the poloidal Mirnov array [36]. All the probe signals are digitized at 100 kHz rate. One of the probes from the toroidal array is acquired simultaneously at 3 MHz rate. This probe will be referred to as 'fast magnetic probe' henceforth in this paper. The poloidal array probes are commissioned in the tokamak through re-entrant tubes inserted from a top port, a bottom port and a mid-plane port. Installation of the probes in re-entrant tubes is required to accommodate the probes in the presence of the LTX-β shell. These three-axes probes are meant for simultaneous measurement in the axial (to the re-entrant tube), perpendicular (to the axial probe) and toroidal components of the magnetic fluctuations. Apart from the Mirnov coils, there are flux loops, diamagnetic loops and Rogowski coils for measuring the loop voltage, stored energy and plasma and coil currents respectively [37].

The single Langmuir probe (SLP) [38] is mounted off-midplane, away from possible interaction with runaway electrons whose distributions typically peaked at the midplane. The SLP is also mounted on a bellows drive, allowing the probe to be inserted to different radial positions in the scrape-off layer (SOL) past the PFC shells. Probe I–V traces are fit to a four-parameter expression to account for sheath expansion that results in non-saturation of ion current evident in the probe data [38].

The LTX-B Thomson scattering (TS) system laser fires once per shot and data from multiple repeated shots are generally averaged to measure electron density and temperature profiles. The TS system is also used to measure time evolution while data from multiple shots are averaged at the same time point to improve statistics. The profiles used in this work are from the core TS system that measures up to 11 radial points in the low field midplane, spanning from the nominal major radius at 40 cm out to 62 cm, which is typically past the last closed flux surface of an inboard limited discharge. The density profiles are re-normalized based on the line averaged density from the 1 mm microwave interferometer measurement along the radial midplane.

An array to sample hydrogen Lyman-α emission is installed in LTX-β for recycling and neutral density estimations [38]. The array comprises a commercial 20 element AXUV photodiode array and a 122 ± 2.5 nm VUV/UV narrow-band filter. The array is installed in the mid-plane and provides nearly reflection-free measurements from the fan-geometry covering more than half of the poloidal extent of the plasma.

2.3. Fueling techniques

There are two different fueling techniques available on the LTX-β: a HFS-GP system and a supersonic gas injector SGI system [38]. Unlike the HFS-GP system, which delivers a prolonged trail of cold neutrals following the actual puff, the SGI system is capable of sharper, sub-millisecond gas pulses, as evident from the sharper density rise following the SGI pulse and instantaneous density fall due to wall pumping by the Li coated shell. HFS-GP is mounted on the center stack a few cm above midplane. SGI is mounted on a top port and is located just outboard of the major axis at 44.5 cm and the nozzle nearly flush with PFC shell.
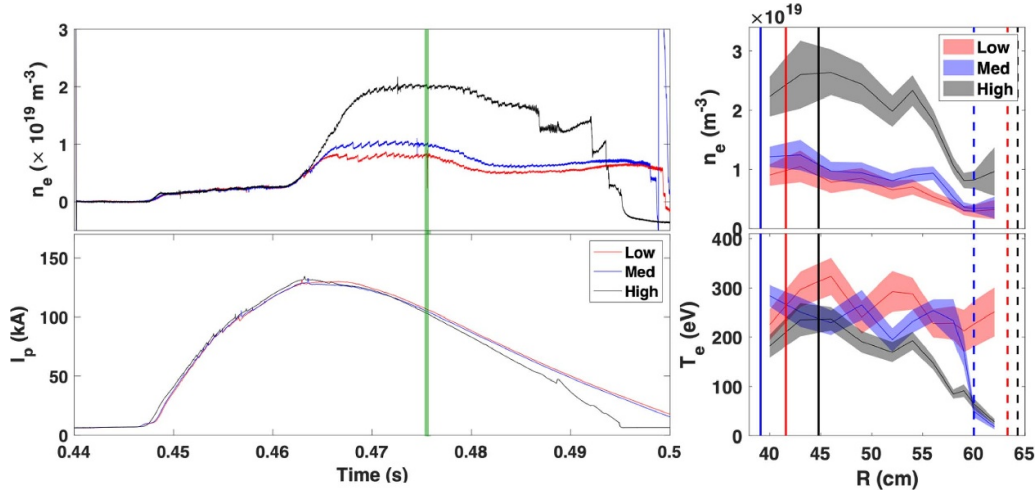
Figure 2. Left: line averaged density and plasma current for the three cases; right: n_e and T_e profiles measured by TS system. Magnetic axis and LCFS are marked with solid and broken vertical lines. Green bar on the left shows the time for the profiles. T_e profile is reasonably flat for the low and medium cases. Extreme low field side points for the medium case might be error prone. Error bars on the profiles represent the multi shot standard deviation and fitting error for the TS data. Last T_e point on the blue curve may be neglected as it is very close to the LCFS and low signal level.

2.4. Plasma profiles

Line averaged density is progressively scanned on a shot-to-shot basis in this experiment to study the excitation threshold of the tearing mode and the flatness of the T_e profile. Three main densities are compared in this paper. One is much higher than the threshold density below which the tearing activity ceases. We call this the high-density case. The other one is near the threshold density limit. We call it the medium-density case. Finally, in the low-density case, the density is below the threshold density. This density threshold is further detailed in section 3. Plasma profiles, obtained from the TS diagnostic [3], in the density flat-top phase, sufficiently away from the gas puff are shown in figure 2. Note that the n_e profile is always peaked with not much change in the peaking factor, which is the ratio of the maximum density in the radial profile to the line averaged density. However, the average density can be controlled precisely with fueling from the edge. In both the low and the medium density cases, T_e profiles are reasonably flat, while in the high case it is peaked. This variation in the n_e and T_e profiles provides a significant variation in the pressure profiles for the high and low cases. Further, the flat T_e profile, and peaked n_e profile also provides an appreciable variation in the plasma resistivity ($\propto T_e^{-3/2}$) and collisionality ($\propto n_e/T_e^2$) profiles across the plasma volume.

3. Tearing mode activity and density threshold

As stated in section 2.4, the line averaged density (n_e^{ave}) is varied progressively from 2.2×10^{19} m^{-3} to 0.5×10^{19} m^{-3}. We are now looking mainly at the density quasi-flat-top phase. Figure 3(*a*) shows the progressive n_e^{ave} decrease achieved by adjusting the HFS-GP pulse length and frequency. The corresponding I_p evolutions for these representative shots are shown in figure 3(*b*). Evolution of I_p is similar for all the shots except

a small dip in the high-density shots. Figures 3(*c*)–(*g*) shows the magnetic fluctuation spectrograms obtained from the fast magnetics probe. It has been observed that at higher densities a strong tearing mode activity is excited in the frequency range of 5–10 kHz just after the plasma current ramp-up phase is completed. At higher densities, often multiple harmonics of the mode are also visible in the spectrograms. As the density is lowered in subsequent shots, the tearing mode activity turns more and more intermittent and eventually ceases to appear when n_e^{ave} goes below $\sim 1 \times 10^{19}$ m^{-3}. Similar results with the same n_e^{ave} threshold for tearing mode destabilization is observed with SGI fueling (not shown here) as well. However, the tailoring of the HFS-GP and the SGI pulse trains is different for maintaining similar n_e^{ave} with these two types of fueling techniques. It can be noted that the high-density cases are susceptible to strong mode growth and mode locking with subsequent disruptions as seen in the high n_e^{ave} plots and the spectrograms in figure 3.

These experiments are done with partially passivated lithium on the machine. Lithium coating on the shell is passivated by previous plasma operations and residual gas, mainly forming compounds with hydrogen (H) and/or oxygen (O). Later the entire set of experiments are repeated with fresh lithium coating too, but the threshold for the tearing modes to appear seems to be robust at $\sim 1 \times 10^{19}$ m^{-3}. With fresh lithium, the wall recycling is expected to be lower [39] and it requires much more gas puffing or SGI pulses to achieve the comparable n_e^{ave}.

Once the density level for exciting the tearing mode is determined, three specific n_e^{ave} cases are selected for further analysis. A high-density case ($n_e^{ave} \sim 2 \times 10^{19}$ m^{-3}), a low-density case ($n_e^{ave} \sim 7.4 \times 10^{18}$ m^{-3}) and a marginal density case ($n_e^{ave} \sim 1 \times 10^{19}$ m^{-3}) near the threshold. As stated in section 2.4, these will be referred to as the high-, low- and medium-density cases respectively from now on.
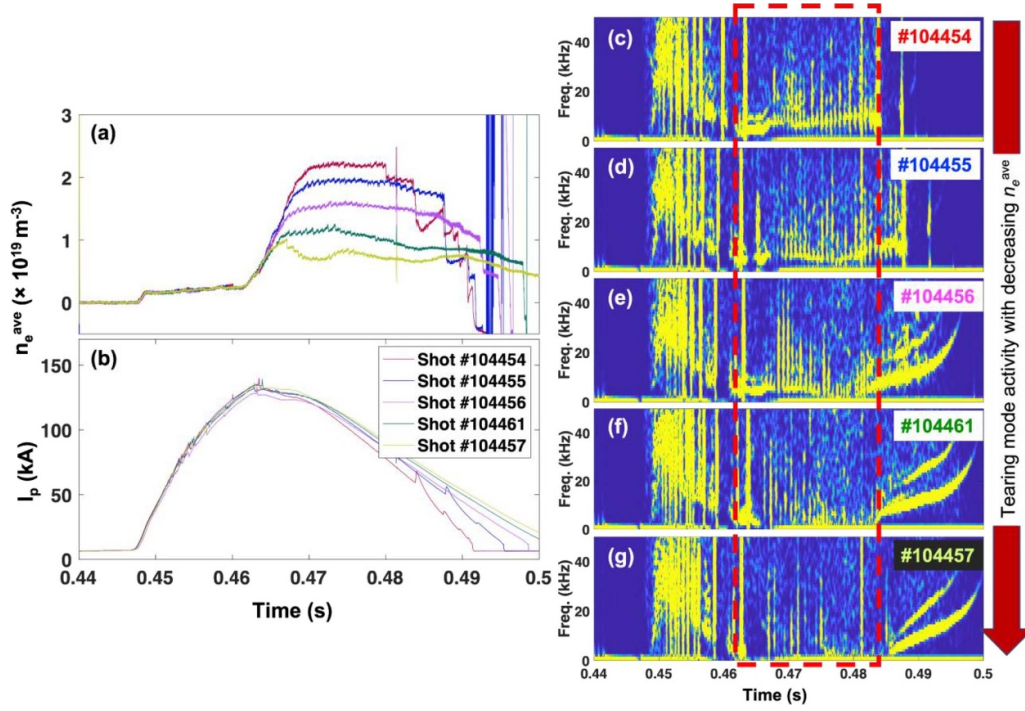
Figure 3. (*a*) line averaged density n_e^{ave} scan for studying the tearing mode evolution and threshold; (*b*) corresponding I_p evolution for the representative shots; (*c*)–(*g*) magnetic spectrograms for the different density cases show that the tearing activity ceases once the line averaged density goes below 1×10^{19} m^{-3}. The red broken rectangle shows the relevant portion of the discharge evolution just after the completion of I_p and n_e^{ave} ramp-up and up to the n_e^{ave} ramp-down or disruption.

Next, we attempt to determine the mode structure of the observed tearing activity. Mode structure of the tearing activity is determined by singular value decomposition (SVD) [40]. Implementing the SVD technique for the toroidal mode number is straightforward as there are 10 probes in the toroidal Mirnov array, well-aligned for the required measurement. However, poloidal mode number analysis is not trivial as several of the three-axes probes in the poloidal Mirnov array are not specifically aligned to measure only the poloidal component of fluctuations. This is because of the re-entrant geometry of these probes. Hence, the poloidal component of the magnetic fluctuations for each probe in the poloidal array is obtained by vector addition of the axial and perpendicular components depending upon their orientation on the vessel wall. In this way 12 of the 20 poloidal array probes are usable as others are discarded either due to malfunctioning of either the axial or the perpendicular probes at that location or poor signal quality. Thus, time series from the 10 toroidal and 12 usable poloidal array probes are used in the SVD analysis. Prior to the SVD analysis the hardware integrated B_θ signals are first corrected for any drifts by subtracting a portion from the 'without plasma' phase and then subtracted with a running average over 2 ms to isolate the fluctuating part of the acquired signals. Thus, the frequency resolution available now in the pre-processed data is greater than 500 Hz. Figure 4(*a*) shows the magnetic spectrogram of a representative high-density case (shot #104463). Corresponding time evolution of the I_p, n_e^{ave} and the pulse train of the HFS-GP are shown in figure 4(*b*). Figure 4(*c*) shows the singular values

plotted in log scale as a function of channels for the representative shot. Figures 4(*d*) and (*e*) show the spatial structure of first two principal axes vs. channels, indicating the $m/n = 2/1$ mode structure for the observed tearing activity, where *m* and *n* are the toroidal and poloidal mode numbers respectively. The toroidal and poloidal mode structures are shown by a single peak and double peaks for the toroidal and poloidal array channels. As stated earlier, the poloidal mode number analysis is non-trivial as a truly poloidally oriented Mirnov garland is not available in LTX-β. In figure 4(*e*) the spatial structure of the first principal axis suggests $m = 2$, while the spatial structure of the second principal axis suggests $m = 3$. Thus, we infer that the toroidal mode number is certainly $n = 1$. However, given the complexity in the diagnostics layout and thereby uncertainty in the poloidal mode number analysis, the poloidal mode number could be 2 or 3. An extreme case of $m = 4$ is also considered later in the M3D-C1 scans.

4. DEGAS 2 simulation of edge neutral density variation

The neutral density profile at the edge is calculated by DEGAS 2 [41] simulations with the help of data from the TS, low field side SLP, Lyman-α array, and magnetics. Toroidal, radial and vertical magnetic field information (B_t, B_r and B_z) are obtained from PSI-Tri [42] equilibrium reconstructions. Profiles of n_e and T_e are obtained from the TS data and T_i is assumed to be $T_e/3$. This assumption is based on the experimental
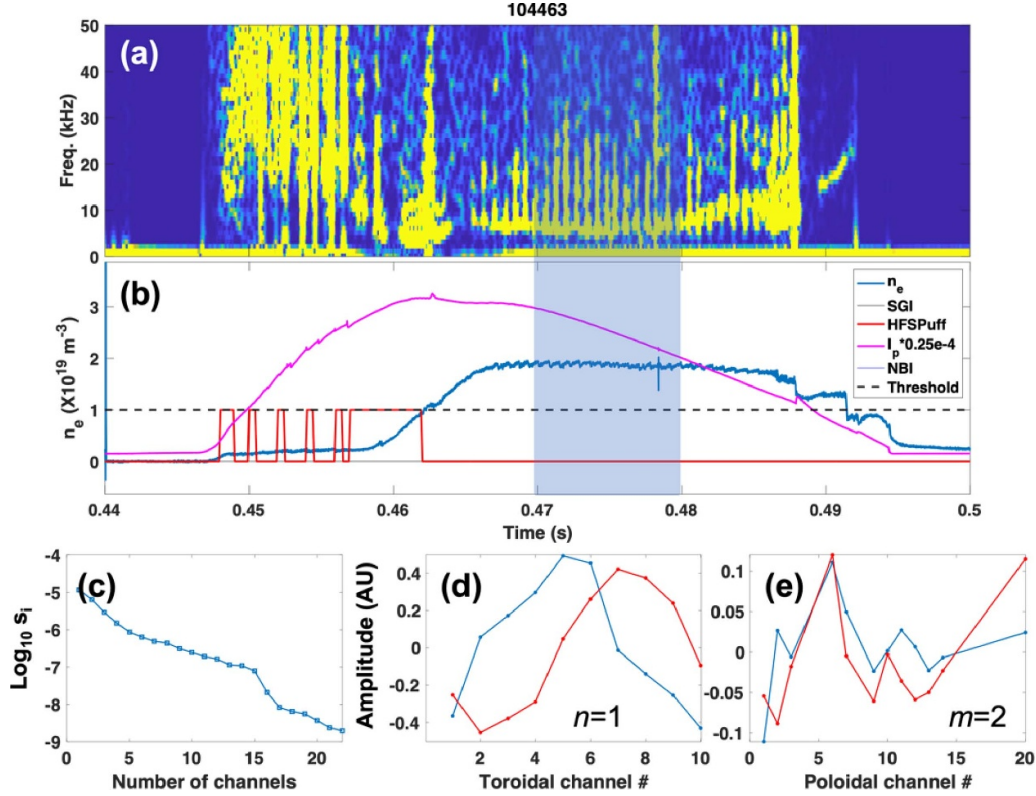
Figure 4. (*a*) Magnetic spectrogram of one of the representative high-density shots; (*b*) time evolution of I_p, n_e^{ave} and HFS-GP pulses. Shaded bar on the spectrogram indicates the time window for the analysis. Note that SGI and NBI are not applied in this shot; the broken black horizontal line in (*b*) denotes the threshold n_e^{ave} of 1×10^{19} m^{-3} (*c*) the singular values are shown; (*d*)–(*e*) toroidal and poloidal mode numbers (*n* and *m*) are estimated from the peaks in the spatial structures of first two principal axes corresponding to the first (red) and the second (blue) singular values vs. toroidal and poloidal channels.

measurements of ion temperature by C VI spectroscopy in similar shots. Here multiple similar discharges are averaged for the TS data to minimize fitting uncertainties. Brightness data for all the diodes in the Lyman-α array are used to constrain the DEGAS2 simulations. The n_e and T_e profiles in open field lines of the SOL are interpolated from the TS data at the edge and the SLP in the SOL. Finally, the geometry file is constructed to represent the wall, last close flux surface and the flux surface coordinates respectively. Figure 5 shows the time evolution of the brightness in two channels of the Lyman-α array, one more towards the core and the other more towards the edge. These two channels are shaded in purple in the diagnostic viewing geometry on the left. It can be observed that the core channel shows a fast rise and saturation in the brightness signal, while the edge channel shows a steady rise with time. The increase in emission after 460 ms denotes the increase in density. Further, the rise in brightness for the high-density case (magenta) is significantly higher compared to the medium (blue) and low-density (green) cases respectively.

DEGAS2 simulation shows significantly high neutral inventory buildup in the high-density case compared to the medium and low-density cases, as shown in figure 6. This supports our hypothesis that the excess neutral inventory in the high-density case is causing the edge cooling and peaking of the T_e profile. This edge cooling might be a plausible explanation of the excitation of the tearing mode [20, 28] as well.

These discharges were initiated on partially passivated lithium PFCs, with at least 4 months old lithium coatings, plenty of time for the lithium on the shells to passivate [43]. Flat temperature profiles were observed in-spite of that, indicating some reduction in recycling. Further, analyses comparing discharges with partially passivated Li and fresh Li PFCs indicate a relative reduction of $\sim$70%–80% in recycling coefficient from passivated to fresh Li PFCs [39].

5. Tearing stability with M3D-C1

The classical tearing stability of these shots is analyzed with the M3D-C1 extended-MHD code [44] using a linear, single-fluid resistive model including a model of the conducting wall. Here the two extreme cases (high- and low-density) are considered. First, the equilibrium reconstruction obtained from the PSI-Tri code is solved again using the internal Grad–Shafranov solver within M3D-C1 to ensure a smooth equilibrium. Figure 7 shows the equilibrium toroidal current density (J_ϕ) distributions, the safety factor (q) and the pressure (p) profiles of the reconstructed equilibria for the two cases. Because the Grad–Shafranov solution depends on the pressure but not on the density and temperature separately, the experimental T_i, T_e, and n_e profiles need to be provided to M3D-C1 in order to get an accurate resistivity profile. This step is particularly
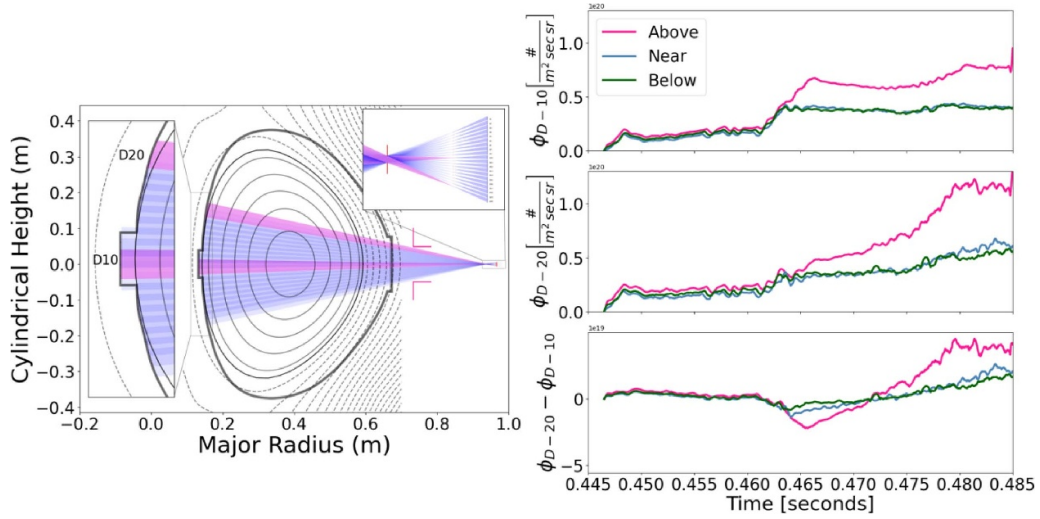
Figure 5. Left: viewing geometry and line of sights (LOS) for the Lyman-α array overlaid on a poloidal cross section of the LTX-β and the medium density shot's equilibrium reconstruction during the density flat-top. The magenta LOSs denote the core (D10) and edge channel (D20); right: time evolution of the line integrated Lyman-α signal in the core (top) and edge (middle) chords and their difference (bottom). The above, near and below labels correspond to high, medium and low-density cases.
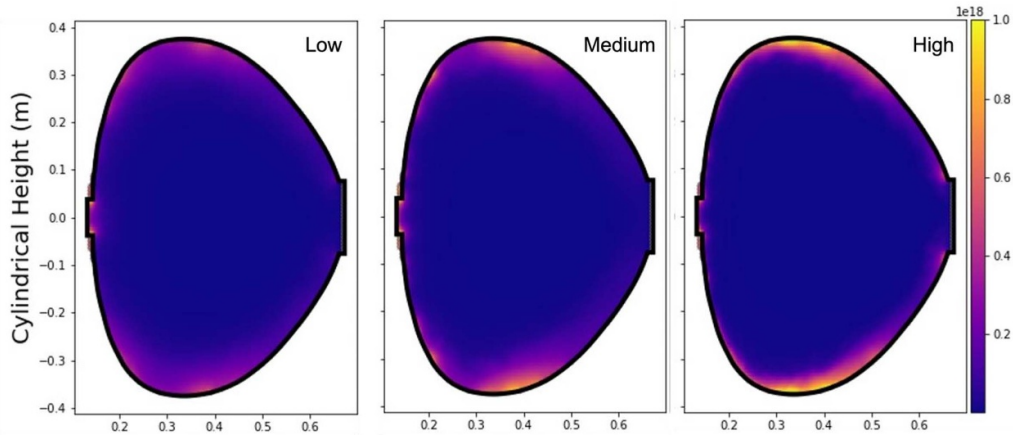

Figure 6. Neutral distribution calculated from the DEGAS2 for the three cases shows significantly higher neutral inventory at the edge for the high-density case. The discharges primarily limit on the high field side. DEGAS2 predicts neutral density buildup at the top and bottom where open field lines intersect with the shells at oblique angles.

important to represent the nearly flat T_e profile scenario for the low-density case. Figure 8 shows the adjusted profiles for the M3D-C1 simulations and the experimental profiles for the high and the low-density cases.

In the first set of simulations a single-fluid resistive MHD model with no equilibrium rotation and no conducting shell are considered. Further, Spitzer resistivity is assumed. In these calculations, we only consider the $n = 1$ modes, which are independent from other toroidal mode numbers because the equilibrium is axisymmetric. In this model both equilibria are observed to be unstable to a $n = 1$ mode as shown in the toroidal current density (J_φ) and p contours in figure 9. The growth rate of the $n = 1$ mode is $\sim$10 times more in the high-density case compared to the low-density case.

The $n = 1$ mode is found to be unstable (the energy grows exponentially) and has broad poloidal mode spectrum and broad radial extent in both these cases as shown in figure 9

(bottom panels). This broad poloidal spectrum is not evident from the experimental observations. It might be the case that the saturated state is dominated more by a single poloidal mode number, but this will require nonlinear simulations. It is also the case that the magnetic diagnostics will preferentially detect lower-m components since these components decay more slowly with distance from the plasma. In general, the internal poloidal mode spectrum is challenging to measure with magnetics diagnostics in toroidal devices, especially at low aspect ratio, due to the radial dependence of the spectrum. The mode is calculated to grow on resistive timescales, with growth rates significantly lower than an inverse Alfvén time. In the high-density case, the mode seems to have an ideal-like character at the 2/1 surface, with the normal, resonant component of the perturbed magnetic field nearly vanishing at the mode-rational surface, but the eigenmode is fundamentally resistive, with nonzero resonant components at other
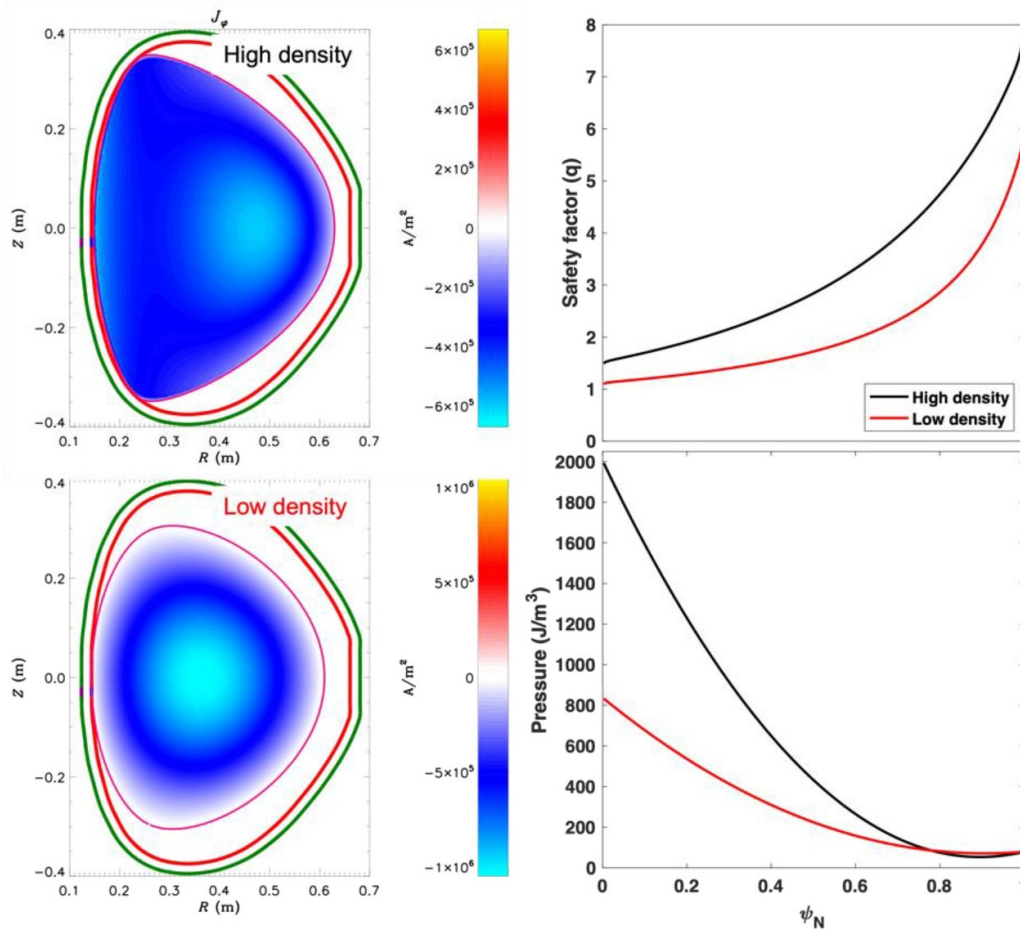
Figure 7. Left: reconstructed equilibrium J_ϕ of the high and low-density cases in the M3D-C1 code; the green and red contours represent the outer and inner surfaces of the copper shell in the M3D-C1 model. Note that while these regions are continuous, the poloidal breaks are included in the model by introducing a large resistivity at the position of the breaks. Right: safety factor (q) and pressure (p) profiles as a function of the normalized flux coordinate (ψ_N) for the high and low-density cases. Note that the q-profile shows significant variation, though available measurements do not provide any local constraints on the current density profiles.

mode-rational surfaces and with a resistive-timescale growth rate that scales with the plasma resistivity.

In the next set of simulations, a conducting shell is added. The conducting shell in the model is modeled as axisymmetric and does not include the toroidal cuts (the poloidal gaps at the midplane are included by treating these as wall regions with very high resistivity). Therefore, this model likely overestimates the stabilizing effect of the shell. Indeed, it is observed that the presence of the conducting shell is stabilizing in both cases. However, the growth rate of the $n = 1$ mode is still more than twice as large in the high-density case compared to the low-density case. Finally, rotation is added in the third set of simulations. The plasma rotation velocity is not well diagnosed in LTX-β, so here we arbitrarily consider the case in which the kinetic energy density from rotation is 1% of the thermal energy density at the magnetic axis: $\frac{1}{2}m_i n_i R_0^2 \omega^2 = 0.01p$. Thus, $\omega(\psi) \sim \sqrt{\frac{p(\psi)}{n(\psi)}}$. Here m_i is the ion mass, n_i is the ion density, R_0 is the major radius, ω is the toroidal angular rotation frequency, and p is the pressure. In discharges 105 923 (high-density) and 105 931 (low-density) this yields a rotation frequency at the magnetic axis of 32 krad s^{-1} and 6.2 krad s^{-1}, respectively. Note that, since LTX-β does not

have data from rotation diagnostic at present, we chose these rotation profiles to explore the potential effect of rotation on the stability of these modes. We picked a value for the magnitude of the rotation that we expected to be fast enough to have an impact on resistive modes but not so large as to affect the equilibrium. However, to put this choice of rotation into perspective, it can be mentioned here that the mode rotation frequency observed in figure 3 is ~6 kHz (or ~38 krad s^{-1}). In this case, the mode in both the high- and low-density cases stabilizes with the addition of rotation. Both the cases appear to be in the 'resistive plasma/resistive wall' regime. Figure 10 shows that the stabilizing eddy currents become visible with the addition of the conducting wall and rotation.

Table 1 shows the scans performed with the conducting shell and plasma rotation for both of these cases. Both cases have decent growth rates of the $n = 1$ mode in the 'no conducting shell' and 'no plasma rotation' simulations. However, the growth rate in the high-density case is about an order of magnitude higher compared to that in the low-density case. This indicates that the flatter T_e profile, which is achieved due to lesser edge cooling, might be stabilizing the mode growth in the low-density case. This is consistent with the experimental
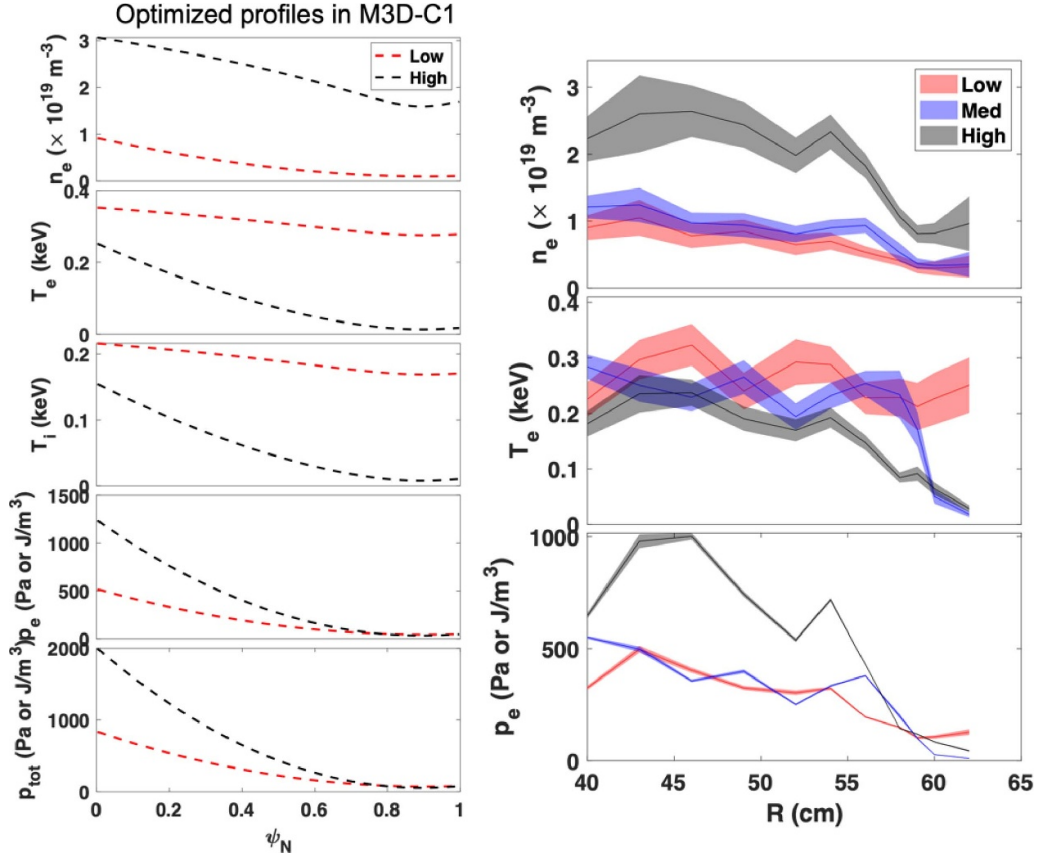
Figure 8. Left panels show the input profiles for the M3D-C1 simulations. Right panels show the experimental profiles from the TS system. LCFS is at 63 cm.
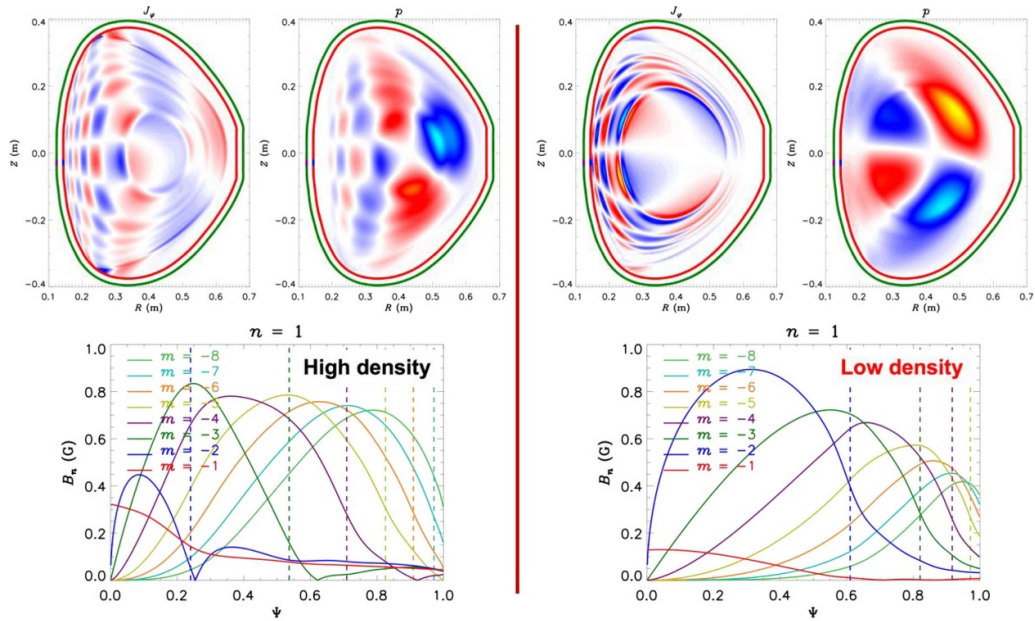

Figure 9. Top row: mode structure visible in both the high (left) and low-density (right) shots in the respective current density and pressure perturbations; bottom row: amplitude of the various poloidal Fourier components of the normal component of the perturbed magnetic field as a function of radius. Mode rational surfaces are indicated by the vertical dashed lines.

findings. Given that the growth rate of the $n = 1$ mode is significantly lower in the low-density case and the added rotation is also significantly lower in the low-density case, compared to the high-density case, the low-density case is more likely to get stabilized with the addition of the conducting shell and the plasma rotation.
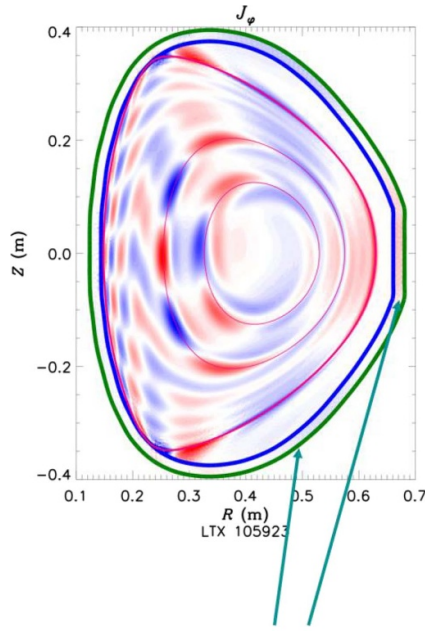
Stabilizing eddy currents visible in
case with wall and rotation

Figure 10. Mode structure in the current density perturbations. Stabilizing eddy currents are visible in the simulation that includes conducting shell and plasma rotation.

Table 1. Detail of the scans with conducting shell and plasma rotation.

Conducting shell	Plasma rotation	Growth rate	
		High-density	Low-density
No	No	5.6 kHz	0.6 kHz
Yes	No	0.7 kHz	0.3 kHz
Yes	Yes	<0 (stable)	<0 (stable)

Destabilization of the tearing activity can be due to the difference in either the pressure profile, or the q profile or both and resistivity. To ascertain further the effect of q profile in terms of the stabilizing effect on the tearing activity, we scanned down the q profile of the high density shot to match the q profile of the low density shot as closely as possible. In all the scans henceforth, the cases shown in figure 9 are taken as starting points and the effects of conducting wall and rotation are excluded. This is done using the Bateman scaling which essentially scales the toroidal field while keeping the current profile fixed [45]. Also, in the process, the n_e, T_e, T_i and total pressure profiles did not change.

Figure 11(*a*) shows the original (solid black) and scaled (broken black) q profiles for the high-density case and the q profile from the low-density case (red). The scaled q profile for the high-density case and the q profile of the low-density case matches well in terms of q_0 and q_{95} but not exactly in the rest of the normalized flux coordinates. This is the best that can be done while keeping the current profile fixed and keeping $q_0 > 1$ to avoid introducing an internal kink mode. Figure 11(*b*) shows the magnetic shear ($S = \frac{rdq}{qdr}$) for the same three cases. The S profiles from the original low-density case

and either of the original high-density or the q adjusted high-density cases match closely with each other till $\psi_N = 0.7$. This close match in S profiles ensures that the q-scan performed here addresses the dependence of the growth rate on the q profile (and hence S) adequately. It can be noted here that the magnetic shear itself cannot be varied independently in the simulation and hence, a magnetic shear scan is not trivial. Further, the n_e, T_e and p profiles of these cases are also shown in figures 11(*c*)–(*e*). Note that the n_e, T_e and p profiles for scaled q profile high-density case (broken black) coincide exactly with the original high-density case (solid black). The growth rates of the three cases are shown in the table in inset. With the scaled down q profile for the high-density case, the growth rate increases even more and now the growth rate in the scaled q profile high-density case is $\sim$15 times that of the low-density case. This further suggests that the stabilization of the tearing mode in the low-density case is indeed due to the change in the resistivity or the pressure profile, mainly influenced by the achievement of the flat T_e profile.

To investigate further the effect of the flat T_e profile on the growth rate of the tearing mode, another scan is done with the low-density case where the T_e profile is modified to a peaked profile. In this case, the p profile and the q profile are kept constant. Consequently, the n_e profile also changed to accommodate for the peaked T_e profile with lower central electron temperature. Figure 12 shows the original (red. solid) and modified n_e and T_e (red, broken) profiles and a comparison of the growth rates. Growth rate of the tearing mode increases by $\sim$5 times when the T_e profile is modified to a peaked profile from the original flat profile. Note that this is a resistive tearing mode as discussed earlier and hence, is expected to grow with resistivity. With flatter T_e and lower n_e, one can expect a weaker growth of the mode as resistivity decreases substantially. However, there are still two effects that appear to destabilize (stabilize) the tearing mode in the high-density case (low-density case), like the flatness of the T_e profile (and hence the pressure profile) and the resistivity. Both these factors could be responsible for this effect and inter-related, while one could be more dominant than the other.

To demonstrate the dominant factor between the change in resistivity and T_e profile variation (peaked or flat) and hence pressure profile variation, another scan is performed. Here the low-density case is taken, and the resistivity is scanned artificially without modifying the q-profile or the n_e, T_e profiles. First, we tried to match the resistivity of the low-density flat T_e case with the low-density peaked T_e case from the last scan shown in figure 12. Resistivity is matched at $\psi_N = 0.61$ which is the $q = 2$ surface for the low-density case. The growth rate obtained (2.8 kHz) matches exactly with the low-density peaked case. Hence resistivity variation is indeed a major factor as expected.

To determine whether the pressure peaking affects the growth rate separately from the resistivity, we scanned the resistivity of the low-density flat T_e case, such that the resistivity matches at $\psi_N = 0.54$ and $\psi_N = 0.7$ with the resistivity of the high-density case. Note that $\psi_N = 0.54$ and $\psi_N = 0.7$ are the $q = 3$ and 4 surfaces of the high-density case respectively. The $q = 4$ match is included to account for the extreme
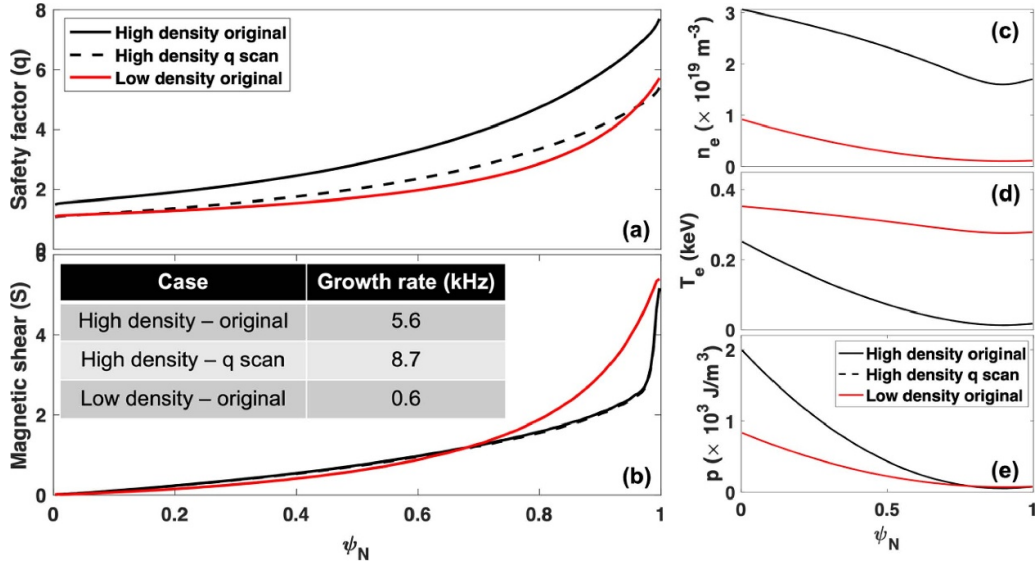
Figure 11. (*a*) and (*b*) The original and scaled q profiles and magnetic shear (S) profiles for the high-density case and the q and S profiles from the low-density case; (*c*)–(*e*) n_e, T_e and p profiles of these cases. Note that the n_e, T_e and p profiles for scaled q profile high-density case (broken black) coincide exactly with the original high-density case (solid black).
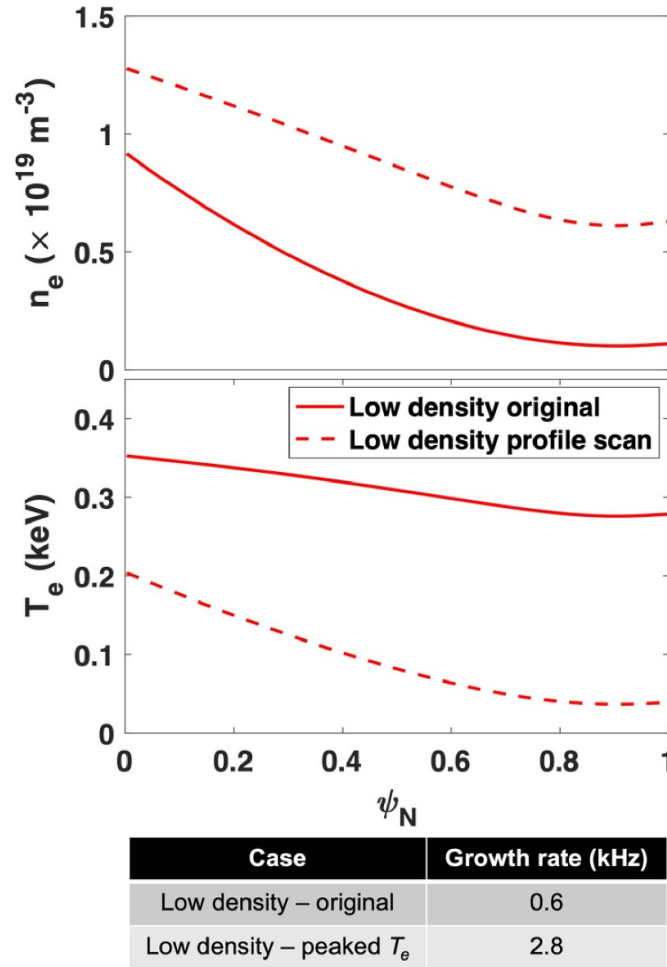

Figure 12. Original (solid) and modified (broken) n_e and T_e profiles to show the change in tearing mode growth rates as an effect of the shift T_e profile from flat to peaked. The growth rates are shown in the bottom panel.
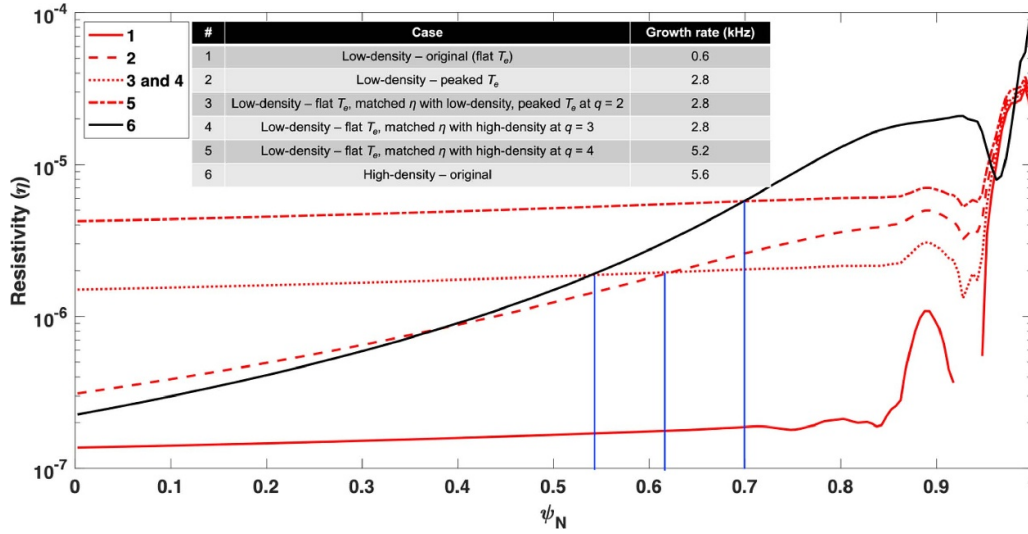
Figure 13. Resistivity (η) for low-density and high-density original cases are shown along with low-density peaked T_e case and η—scans of the low-density case while match at different mode rational surfaces. Inset shows the legend of the plots and the respective growth rates of these cases.

uncertainty case in determining the poloidal mode number of the tearing mode as discussed earlier in section 3. Note that in these scans, the resistivity is significantly larger than in the high-density case at $\psi_N = 0.2$, which is the location of the $q = 2$ surface. Figure 13 shows the resistivity scans and the growth rates in the inset. When the resistivity is matched at the $q = 3$ surface ($\psi_N = 0.54$) the growth rate is only 2.8 kHz, a factor of 2 lower than the growth rate for the high-density case (5.6 kHz). Even for the extreme case of resistivity matching at $q = 4$ surface the growth rate is 5.2 kHz, which is still lower than the high-density case. This shows that the flattening of the pressure profile resulting from the flat T_e profile stabilizes the tearing mode independently from the reduction of resistivity.

Finally, to emphasize the effect of profile flatness on the growth rate, we started with the high-density case where the q-profile is adjusted to resemble the q-profile of the low-density case. This case is shown earlier in figure 11 and has a growth rate of 8.7 kHz. Now we decreased the resistivity of this case such that the resistivity matches with that in the original flat T_e profile low-density case at the mode rational surface of $q = 2$. The obtained growth rate in this η-adjusted case turns out to be 2 kHz. Hence, the growth rate is 4.5 times less than the modified-q high-density case (8.7 kHz) but 3 times more than the original flat T_e profile low-density case (0.6 kHz). This result emphasizes the observations as: (1) the decrease in resistivity shows a 4.5 time decrease in the growth rate, so, for a given q profile, resistivity is an important factor for the stability of the tearing more, as expected for resistive tearing modes and (2) since the main difference is in the pressure profile, due to the difference in the n_e and T_e profiles and more precisely, the flatness of the pressure profile, mostly due to the flatness of the T_e profile, once the q profile and the resistivity at the mode rational surface are similar, the flat T_e profile is even more stabilizing for the tearing modes as the growth rate in this new resistivity-adjusted high-density case is still three times more than the flat T_e low density-case.

To summarize the scans, growth rate depends on three main factors: the q profile, the resistivity at the mode rational surface and the flatness of the pressure profile. Now, T_e and the corresponding n_e can influence two of these three factors as the resistivity and the flatness of the pressure profile. For the same pressure profile and resistivity at the mode rational surface, a flatter q profile will provide higher growth rate (refer to figure 11). Given the q profile and the resistivity at the mode rational surface are similar, a more peaked pressure profile can result into higher growth rate (refer to the comparison of original low-density case and the q- and η-adjusted high-density case). Finally, if the q profile and the pressure profile are similar, higher resistivity at the mode rational surface will result into higher growth rate (refer to the η-adjusted low-density flat and peaked T_e cases). A flatter T_e profile will provide a flatter pressure profile and/or a lower resistivity at the mode rational surface, thus stabilizing the tearing mode.

6. Study of fast-ion loss due to the tearing activity

Loss of fast ions by tearing modes is a matter of great concern in future reactor grade plasmas as fast ions are expected to play a vital role in self-sustaining ignition. In LTX-β, however, the concern is solely about the confinement of the fast ions produced by the neutral beam and hence the efficiency of the neutral beam heating. To study the possible effect of tearing mode activity on the fast ion confinement we started again with the PSI-Tri generated kinetic equilibria and generated the magnetic field perturbation ($\delta B_r/B$) representing a 2/1 mode in the ORBIT code [46], as shown in figure 14(*a*).

The mode amplitude is scaled in ORBIT to quantify the fractional loss of fast particles as a function of the mode strength. The initial fast-ion distribution is taken from the NUBEAM-TRANSP [47] run for a representative neutral beam injected shot. It has been observed that very few fast particles ($<5\%$) are lost even at large mode amplitude,
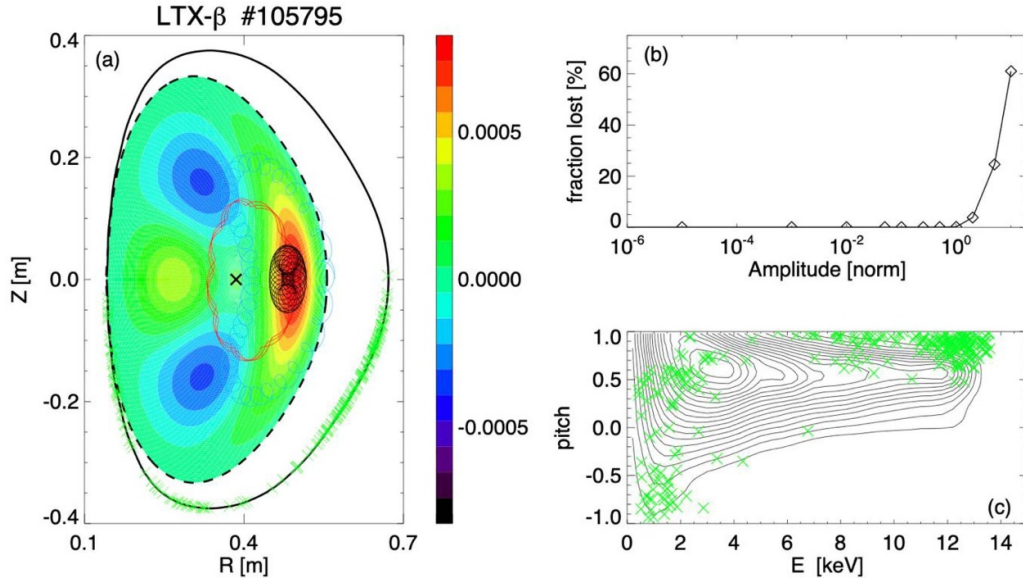
Figure 14. (*a*) Poloidal cross section with contours of the radial magnetic field perturbation normalized to the background field for a 2/1 tearing mode. Amplitude corresponds to a normalized $A = 1$ in ORBIT. Green crosses indicate fast ions lost on the wall. The dashed line shows the LCFS and the solid line the shells. Colored lines indicate orbits for co-passing (red), stagnation (black) and trapped (light blue) NB ions with energy $\sim$12 keV. While ORBIT computes the particles' orbit using a guiding-center approach, reconstructed full-orbits are shown including the instantaneous particle location accounting for finite Larmor radius. (*b*) Lost NB ion fraction as a function of the normalized tearing mode amplitude. (*c*) Core fast ion distribution from NUBEAM (contour lines). Green crosses indicate fast ions that are eventually lost following interaction with the 2/1 tearing mode.

corresponding to a perturbation of the radial magnetic field $\delta B_r/B \sim 10^{-3}$ with respect to the equilibrium magnetic field (see figure 14(*b*)). This is mainly due to the large orbits of the fast ions because of the low magnetic field, which is a characteristic of spherical tokamaks like LTX-β. Hence, even if the fast ions are affected locally by the mode islands, they are not thrown out of the plasma.

Based on ORBIT simulations, co-passing and stagnation orbits are the most affected by tearing activity, while trapped particles are not because of the limited spatial overlap between fast ion orbits and peaks of the perturbation. Incidentally, finite orbit width (FOW) effects, captured by the guiding-center formalism adopted in ORBIT, seem to be more important than finite Larmor radius (FLR) effects for this scenario. For the low magnetic field of LTX-β, fast ion orbit widths can be comparable to the extent of the radial perturbation caused by tearing modes, while the Larmor radius—although it is a significant fraction of the minor radius—typically remains smaller than that (figure 14(*a*)). Future simulations will further explore the relative significance of FOW vs. FLR effects in LTX-β and other compact ST configurations. Only for relative perturbation amplitudes $\delta B_r/B \sim 10^{-2}$ or larger significant fast ion losses are observed, mostly affecting co-passing particles with energy >7–8 keV (see figures 14(*b*) and (*c*)). However, should the mode achieve such a large amplitude, those amplitudes are likely to result in locking and disruption of the plasma, which is clearly of greater concern than fast ion confinement. In future studies, loss and redistribution of thermal ions due to tearing activity will be also evaluated in the same way with the ORBIT code by suitably replacing the fast ion distribution with bulk ion distribution.

7. Summary and discussions

The role of neutrals in determining the MHD stability of the plasma in LTX-β is investigated. Further, the role of neutrals is documented for the first time at the edge/SOL of the plasma in determining the achievability of the flat T_e profiles. Note that the achievability of the flat T_e profiles is a unique feat demonstrated earlier by ultra-low wall recycling regime of operation in the LTX-β tokamak. Strong interplay between the MHD stability and achievability of flat T_e profile, in response to the edge neutral inventory is established. It has been observed that beyond a critical limit of fueling, the T_e profile tends to peak and the neutral inventory at the edge grows significantly as confirmed by DEGAS2 simulations. As a result of the enhanced neutral inventory of the edge, the edge T_e cools off considerably resulting in a peaked T_e profile. Further, the edge cooling phenomena excites strong resistive tearing activity which has the potential to cause confinement degradation and eventually disruptions. The tearing mode characteristic is analyzed with SVD technique to indicate the $m/n = 2/1$ structure. It can be noted here that the toroidal mode number is inferred certainly as $n = 1$. However, due to the complexity in the poloidal Mirnov array layout and thereby uncertainty in the poloidal mode number analysis, the poloidal mode number could be 2 or 3. An extreme case of $m = 4$ is also considered later in the M3D-C1 scans.

The unique low recycling operation regime of LTX-β provides the opportunity to comprehensively document the role of neutrals, which is otherwise difficult in present-day tokamaks operating with high recycling coefficients. The reason behind this success is that in LTX-β, density can be

evolved in a much more controlled fashion with external fueling techniques when the wall with low recycling coefficient is pumping out strongly. Due to low recycling from the walls, the critical fueling limit for edge cooling, T_e profile shift from flat to peaked and excitation of tearing mode is manifested much more precisely as a n_e^{ave} threshold in the experiments in LTX-β, in contrast to other operational present-day tokamaks. Fueling the reactor grade plasmas, which manifests collision-less or low collisionality (and high opacity) regime, from the edge is a challenge and the behavior of the edge and pedestal in response to edge fueling under these conditions is an outstanding issue. Earlier, integrated core-edge plasma simulations of ITER scenarios showed that at higher electron density, reduced ionization inside the separatrix will strongly limit the formation of the pedestal density profile [48]. However, recently, SOLPS-ITER simulations for Alcator C-Mod in ITER-like opaqueness conditions revealed that electron density pedestal structure will not be affected by increased edge fueling [49]. Our results of destabilization of the tearing mode and change in the T_e profile due to edge fueling might add to the perspective of MHD stability of low-collisionality regime of operation with edge fueling.

M3D-C1 simulations predict that both the high and the low-density plasmas are prone to the excitation of the $m/n = 2/1$ tearing mode and thus supporting the experimental observations. Consistent with the experimental findings M3D-C1 predicts that the high-density case is ten times more susceptible to the mode growth compared to the low-density case. Resistive character of the tearing mode is established as the growth rate scales with plasma resistivity. Further, the stabilizing role of conducting wall and plasma rotation is also observed. However, since the growth rate is ∼10 times lower for the low-density case, compared to the high-density case, even when the conducting wall and plasma rotation are not included, several scans are performed with M3D-C1 to untangle the effects of the other major factors that can influence the growth rate. These factors include, the pressure profile, the q profile (and hence the magnetic shear) and resistivity.

A q profile scan for the high-density case shows that the growth rate of the mode is even larger if the q profile of the high-density case is scaled as closely as possible to the low-density case. Note that in this q profile scan, the magnetic shear is matched appreciably well (up to $\psi_N = 0.7$) between the high-density case (both original and q-adjusted) and the low-density case. The magnetic shear itself cannot be varied independently in the simulation and hence, a magnetic shear scan cannot be performed. Further, the scan showing a shift of the T_e profile from flat to peaked results in a five-fold increase of the tearing mode growth rate in the low-density case. Hence, the difference in the pressure profile for the low-density case, mostly influenced by the flatness of the T_e profile, could be a plausible reason behind the stabilization of the mode in the low-density case, compared to the high-density case. The mode growth in the high-density case could be strongly enhanced by the peaked T_e profile, observed due to edge cooling by the larger neutral inventory at the edge.

To gain further insight into this observation, a few more scans are performed. First the resistivity of the original flat T_e profile low-density case is increased artificially to match the resistivity of the peaked T_e profile low-density case at the mode rational surface and the growth rate was found to match the peaked T_e profile low-density case. This shows that resistivity is indeed a governing factor as expected for the resistive tearing modes. Then the resistivity of the original flat T_e profile low-density case is increased to match the resistivity of the high-density case at mode rational surfaces at $q = 3$ and $q = 4$. Here the resistivity is much higher than at the $q = 2$ surface. The mode growth in this scan increases but remains lower than the high-density case. This indicates the importance of the flatness of the pressure profile, mainly due to the flatness of the T_e profile. Finally, the case where the q-profile of the high-density case is adjusted to match that of the low-density case is taken and the resistivity is adjusted to match that of the low-density case at the mode rational surface ($q = 2$). In this case the growth rate decreases but remains much higher compared to that in the low-density case. We can infer from these scans that the flatness of the T_e profile not only lowers the resistivity at the mode rational surface but also provides the flatness of the pressure profile. Thus, a flat T_e profile is more likely to stabilize the tearing mode growth rate through these two factors.

These observations might lead to the conjecture that if the edge cooling via edge neutrals can be minimized, say by some means of core fueling like pellet injection, flat T_e profile can be achieved even in the high-density case and consequently tearing modes can be stabilized. Core fueling via pellet injection is not trivial in LTX-β, given the small volume of the plasma. However, achieving flat T_e profile and stabilization of tearing activities through broader pressure profile could very well be possible in bigger tokamaks or reactor grade machines via core fueling, if the low wall recycling route is explored. As stated earlier, this route can then serve as a game changer for compact fusion endeavors like the proposed fusion pilot plant [50, 51] because flat temperature profiles will ensure reduced temperature gradient driven turbulence and turbulence driven transport, and hence improved confinement and bigger plasma volume conducive for fusion to happen.

Last but not the least, even though these tearing activities could be disruptive in the high-density plasmas, yet they pose no significant threat to the fast-ion population from the neutral beam as confirmed by the ORBIT-Kick simulations. This is attributed to the large fast-ion orbits due to the low magnetic field of the spherical tokamak LTX-β.

Acknowledgments

ORCID iDs

Santanu Banerjee ![ORCID] https://orcid.org/0000-0003-0859-8855

D.P. Boyle ![ORCID] https://orcid.org/0000-0001-8091-8169

A. Maan ![ORCID] https://orcid.org/0000-0001-7474-2785

N. Ferraro ![ORCID] https://orcid.org/0000-0002-6348-7827

R. Majeski ![ORCID] https://orcid.org/0000-0001-9437-0958

M. Podesta ![ORCID] https://orcid.org/0000-0003-4975-0585

R. Bell ![ORCID] https://orcid.org/0000-0001-9544-498X

C. Hansen ![ORCID] https://orcid.org/0000-0001-6928-5815

W. Capecchi ![ORCID] https://orcid.org/0000-0002-0380-0180

D. Elliott ![ORCID] https://orcid.org/0000-0003-4535-0381

References

[1] Boyle D., Majeski R., Schmitt J., Hansen C., Kaita R., Kubota S., Lucia M. and Rognlien T. 2017 *Phys. Rev. Lett.* **119** 015001

[2] Boyle D. *et al* 2021 *Proc. 47th EPS Conf. On Plasma Physics* (*Virtual conference, 21–25 June 2021*) (available at: http://ocs.ciemat.es/EPS2021PAP/pdf/P1.1023.pdf)

[3] Boyle1 D.P. *et al* 2023 *Nucl. Fusion* **63** 056020

[4] Krasheninnikov S.I., Zakharov L.E. and Pereverzev G.V. 2003 *Phys. Plasmas* **10** 1678

[5] Zakharov L.E. 2019 *Nucl. Fusion* **59** 096008

[6] Majeski R. *et al* 2017 *Phys. Plasmas* **24** 056110

[7] Guttenfelder W., Candy J., Kaye S.M., Nevins W.M., Wang E., Bell R.E., Hammett G.W., LeBlanc B.P., Mikkelsen D.R. and Yuh H. 2011 *Phys. Rev. Lett.* **106** 155004

[8] Moradi S., Pusztai1 I., Guttenfelder W., Fülöp T. and Mollén A. 2013 *Nucl. Fusion* **53** 063025

[9] Rafiq T., Kaye S., Guttenfelder W., Weiland J., Schuster E., Anderson J. and Luo L. 2021 *Phys. Plasmas* **28** 022504

[10] Rafiq T., Wilson C., Luo L., Weiland J., Schuster E., Pankin A.Y., Guttenfelder W. and Kaye S. 2022 *Phys. Plasmas* **29** 092503

[11] Dorland W., Jenko F., Kotschenreuther M. and Rogers B.N. 2000 *Phys. Rev. Lett.* **85** 5579

[12] Jenko F., Dorland W. and Hammett G.W. 2001 *Phys. Plasmas* **8** 4096–104

[13] Zocco A., Xanthopoulos P., Doerk H., Connor J.W. and Helander P. 2018 *J. Plasma Phys.* **84** 71584010 (available at: https://scholar.google.pt/scholar?oi=bibs& cluster=10074532575680956494&btnI=1&hl=en)

[14] Casati A., Bourdelle C., Garbet X. and Imbeaux F. 2008 *Phys. Plasmas* **15** 042310

[15] Ryter F., Angioni C., Peeters A.G., Leuterer F., Fahrbach H.-U. and Suttrop W. (ASDEX Upgrade Team) 2005 *Phys. Rev. Lett.* **95** 085001

[16] Connor J.W., Hastie R.J. and Helander P. 2006 *Plasma Phys. Control. Fusion* **48** 885–900

[17] Rettino B., Hayward-Schneider T., Biancalani A., Bottino A., Lauber P., Chavdarovski I., Weiland M., Vannini F. and Jenko F. 2022 *Nucl. Fusion* **62** 076027

[18] Chavdarovski I., Schneller M. and Biancalani A.J. 2021 *Plasma Phys.* **87** 905870408

[19] Chavdarovski I. and Zonca F. 2009 *Plasma Phys. Control. Fusion* **51** 115001

[20] Suttrop W. *et al* 1997 *Nucl. Fusion* **37** 119

[21] Teng Q., Brennan D.P., Delgado-Aparicio L., Gates D.A., Swerdlow J. and White R.B. 2016 *Nucl. Fusion* **56** 106001

[22] Sauthoff N.R., Von Goeler S. and Stodiek W. 1978 *Nucl. Fusion* **18** 1445

[23] Tsuji S., Nagayama Y., Miyamoto K., Kawahata K., Noda N. and Tanahashi S. 1985 *Nucl. Fusion* **25** 305

[24] Alladio F. and Crisanti F. 1986 *Nucl. Fusion* **26** 1143

[25] Wesson J.A. *et al* 1989 *Nucl. Fusion* **29** 641

[26] Waidmann G. and Kuang G. 1992 *Nucl. Fusion* **32** 645

[27] van Milligen B.P., van Lammeren A.C.A.P., Lopes Cardozo N.J., Schuller F.C. and Verreck M. 1993 *Nucl. Fusion* **33** 1119

[28] Pucella G. *et al* 2021 *Nucl. Fusion* **61** 046020

[29] Dhyani P. *et al* 2014 *Nucl. Fusion* **54** 083023

[30] Banerjee S. *et al* 2017 *Phys. Plasmas* **24** 102513

[31] Rebut P.H. and Hugon M. 1985 *Plasma Physics and Controlled Nuclear Fusion Research 1984 (Proc. 10th Int. Conf. London, 1984)* (*London 12–19 September 1984*) vol 2 (IAEA) p 197 (available at: www.google.com/url?sa=t& rct=j&q=&esrc=s&source=web&cd=&ved=2ah UKEwiXzJLa98uEAxVCF2IAHW3KBjcQFnoECBMQ AQ&url=https%3A%2F%2Finis.iaea.org%2Fcollection %2FNCLCollectionStore%2F_Public%2F16%2F055% 2F16055667.pdf&usg=AOvVaw2GUdV15Qfd05Z2LIgW bn_0&opi=89978449)

[32] Rutherford P.H. 1984 Resistive instabilities in tokamaks PPPL report-2277 (available at: www.google.com/url? sa=t&rct=j&q=&esrc=s&source=web& cd=&ved=2ahUKEwiZ3aKvvs6EAxVQElkFHfD5Az UQFnoECBEQAQ&url=https%3A%2F%2Finis.iaea. org%2Fcollection%2FNCLCollectionStore%2F_ Public%2F17%2F026%2F17026389.pdf&usg= AOvVaw37AzvCoGDfRsZY0XelAB_8&opi=89978449)

[33] Salzedas F., Schüller F.C., Oomens A.A.M. and The RTP Team 2002 *Phys. Rev. Lett.* **88** 075002

[34] de Castro A., Moynihan C., Stemmley S., Szott M. and Ruzic D.N. 2021 *Phys. Plasmas* **28** 050901

[35] Hughes P.E., Majeski R., Kaita R., Kozub T., Hansen C. and Boyle D.P. 2018 *Rev. Sci. Instrum.* **89** 10J104

[36] Schmitt J.C., Bialek J., Lazerson S. and Majeski R. 2014 *Rev. Sci. Instrum.* **85** 11E817

[37] Berzak L., Jones A.D., Kaita R., Kozub T., Logan N., Majeski R., Menard J. and Zakharov L. 2010 *Rev. Sci. Instrum.* **81** 10E114

[38] Maan A. *et al* 2023 *Nucl. Mater. Energy* **35** 101408

[39] Maan A. *et al* 2024 Estimates of global recycling coefficients for LTX-β discharges *Phys. Plasmas* **31** 022505

[40] Nardone C. 1992 *Plasma Phys. Control. Fusion* **34** 1447

[41] Stotler D. and Karney C. 1994 Neutral gas transport modeling with DEGAS 2 *Contrib. Plasma Phys.* **34** 392–7

[42] Hansen C., Boyle D.P., Schmitt J.C. and Majeski R. 2017 *Phys. Plasmas* **24** 042513

[43] Maan A. *et al* 2021 *Plasma Phys. Control. Fusion* **63** 025007

[44] Ferraro N.M., Jardin S.C. and Snyder P.B. 2010 *Phys. Plasmas* **17** 102508

[45] Bateman G. and Peng Y.-K.M. 1977 *Phys. Rev. Lett.* **38** 829

[46] White R.B. and Chance M.S. 1984 *Phys. Fluids* **27** 2455

[47] Grierson B.A. *et al* 2018 *Fusion Sci. Technol.* **74** 101

[48] Romanelli M. *et al* 2015 *Nucl. Fusion* **55** 093008

[49] Reksoatmodjo R., Mordijck S., Hughes J.W., Lore J.D. and Bonnin X. 2021 *Nucl. Mater. Energy* **27** 100971

[50] FESAC Report 2020 Powering the future (available at: www. google.com/url?sa=t&rct=j&q=&esrc=s&source=web& cd=&ved=2ahUKEwjmz42Lv86EAxUQFmIAHeW- DuYQFnoECBMQAQ&url=https%3A%2F%2Fscience. osti.gov%2F-%2Fmedia%2Ffes%2Ffesac%2Fpdf%2F 2020%2F202012%2FFESAC_Report_2020_Powering_ the_Future.pdf&usg=AOvVaw0zHDG07-rtXk1fm8ur5- 5v&opi=89978449)

[51] National Academies of Sciences, Engineering, and Medicine 2021 *Bringing Fusion to the U.S. Grid* (The National Academies Press) (https://doi.org/10.17226/25991)